Springer

Acta Mechanica Sinica

CrossMark click for updates

• RESEARCH PAPER •

Acta Mech. Sin., Vol. 40, 124270 (2024)
https://doi.org/10.1007/s10409-024-24270-x

Direct FE^2 multiscale simulation of hydrogen diffusion in Zircaloy cladding

Han Zhao[1], Xianghua Zheng[1], Shiting Yang[1], Xin Yang[2*], and Wei Li[3*]

[1] *School of Intelligent Manufacturing, Chengdu Technological University, Chengdu 611730, China;*
[2] *Shock and Vibration of Engineering Materials and Structures Key Laboratory of Sichuan Province, Mianyang 621000, China;*
[3] *Key Laboratory of Deep Earth Science and Engineering, Ministry of Education, College of Architecture and Environment, Sichuan University, Chengdu 610065, China*

Received June 4, 2024; accepted June 11, 2024; published online August 13, 2024

This study utilizes Direct FE^2 multiscale simulation techniques to propose an innovative approach for analyzing hydrogen diffusion in Zircaloy cladding. This method combines finite element simulations at two scales into a monolithic framework by utilizing downscaling rules and scaling factors. Through the investigation, it was found that voids induce non-uniform diffusion of lattice hydrogen, demonstrating a strong correlation between trapped concentration and microstructure. Additionally, the accumulation of trapped hydrogen leads to localized plastic deformation and a reduction in effective diffusivity. Furthermore, two representative volume elements were established to depict the void distribution at various stages of its evolution. It is evident that in the initial phases of void evolution, the hydrogen-induced softening effect facilitates crack propagation deep within the zirconium alloy cladding. Moreover, as void evolution progresses into the second stage, this effect intensifies the incidence of localized damage at the narrow inter-void ligaments.

Direct FE^2, Zircaloy cladding, Hydrogen diffusion, Voids

Citation: H. Zhao, X. Zheng, S. Yang, X. Yang, and W. Li, Direct FE^2 multiscale simulation of hydrogen diffusion in Zircaloy cladding, Acta Mech. Sin. 40, 124270 (2024), https://doi.org/10.1007/s10409-024-24270-x

1. Introduction

The Zircaloy cladding operates in radiation and hydrogen environments and is the first line of protection against nuclear fuel leakage. It encloses fuel pellets, enduring radiation damage induced by high-energy neutron flux. Meanwhile, its outer surface interacts with coolant to generate hydrogen, when excess hydrogen diffuses into the zirconium matrix and forms hydrides (ZrHx), hydrogen embrittlement may occur [1]. The phenomena of hydrogen embrittlement primarily stem from mechanisms like hydrogen-enhanced decohesion and hydrogen-enhanced plasticity, predominantly observed in metallic compounds such as steels. However, in Zircaloy, hydrogen embrittlement is always referred to as hydride embrittlement, since the brittle hydride phase significantly degrades ductility and fracture toughness [2,3]. Additionally, the formed hydride network provides the crack initiation and propagation path, which is responsible for the unexpected sudden brittle fracture of the cladding [4]. Nuclear fuel leakage caused by cladding rupture is the most serious accident in the nuclear power industry. For example, the Fukushima nuclear power plant accident in 2011 has not yet completely eliminated its damage to the environment. Therefore, as the first step in the hydride embrittlement process, grasping the intricacies of hydrogen diffusion lays the groundwork for exploring the hydride embrittlement phenomenon.

As the smallest element, hydrogen easily diffuses into metals via normal interstitial lattice sites (NILS) or dislocation transport, where it can reside at different trapping sites, including dislocations, grain boundaries, and carbide/matrix interfaces, among others [5]. To accurately describe hydrogen diffusion and distribution characteristics, com-

*Corresponding authors. Email addresses: yangxin@swust.edu.cn (Xin Yang); weili@stu.scu.edu.cn (Wei Li)
Executive Editor: Zhuhua Zhang

monly used techniques include molecular dynamics [6,7] and first principles methods [8,9], which are based on the description of interatomic interactions. However, these microscale simulation methods are limited by both spatial and temporal scales, posing challenges in obtaining the macroscopic response of the structure. On the other hand, Sofronis and McMeeking [10] devised a finite element (FE) model to simulate the coupled diffusion and plastic straining, incorporating the effect of crack-tip dislocation trapping. Subsequently, Krom et al. [11,12] reformulated the diffusion model to depict the strain rate-dependent equilibrium hydrogen concentration at NILS and trapping sites. Dadfarnia et al. [13] expanded the model to concurrently simulate multiple trapping types. More recently, the hydrogen diffusion model has been coupled with the phase field method to address coupled mechanical-hydrogen problems [14,15]. These numerical strategies have garnered significant attention as essential prerequisites for the numerical and theoretical research of hydrogen-induced damage mechanisms.

Under irradiation conditions, energetic particles collide with lattice atoms, knocking them out of their lattice sites and leaving vacancies in the material matrix [16]. References [17-19] have shown that hydrogen facilitates the agglomeration of vacancies, resulting in the formation of voids. To investigate the mechanism of ductile fracture promoted by micro-voids, Koplik and Needleman [20] proposed the unit cell approach, allowing for the representation of interactions with neighboring cells through the application of periodic boundary conditions (PBCs). Using this framework, researchers have investigated how hydrogen-void interactions affect void growth, coalescence, and failure mechanisms [21-23]. However, Bandstra and Koss [24] pointed out that infinite arrays cannot completely capture the effects of microstructure failure on the overall structure.

The multi-scale FE method using computational homogenization techniques was first introduced by Smit et al. [25] and termed FE^2 by Feyel and Chaboche [26]. The FE^2 method involves both macroscale and microscale FE calculations in a nested solution procedure. Within this procedure, the substructure is resolved by the representative volume element (RVE) associated with the Gaussian points in the macroscale elements. The information exchange mechanisms of FE^2 allow for the description of macrostructure derived from the material microstructure. In fact, this idea, which utilizes homogenized microscopic information for macroscopic simulations, boasts great flexibility. First, through appropriate homogenization techniques, the true sense of multi-layer simulations can be nested, whereby the superscript "2" in the term "FE^2" can be rewritten as "n". For example, Dang et al. [27] subdivided the RVE of textile composites into unit cells, and then further divided it into equivalent lamina elements. Second, different numerical methods can be employed at different scales. Zhao et al. [28] proposed a multi-level model that couples the finite element method (FEM) with the discrete element method (DEM). In this model, RVEs simulated using the DEM were embedded at the integration points of macroscale elements in FEM. More recently, by substituting the FEM with the material point method (MPM), they achieved bridging of DEM and MPM [29]. The flexibility of the framework holds promise for studying the influence of hydrogen-void interactions on the overall properties of Zircaloy cladding. However, in these mentioned frameworks, the bi-directional reading and writing of data between scales has been shown to require tremendous computational resources, limiting its practical engineering application for large problem domains [30,31]. It was not until 2020 that the Direct FE^2 method, proposed by Xu et al. [31], significantly improved computational efficiency by replacing nested computations with a monolithic framework, establishing the groundwork for large-scale use of this numerical technique.

To study the diffusion behavior of hydrogen in Zircaloy cladding tubes under operating conditions, the Direct FE^2 method has been expanded beyond its initial application in stress analysis to simulate the process of hydrogen diffusion. Following the proposed modeling strategy, a multi-scale cladding tube model has been constructed, enabling exploration of the mutual influence between voids induced by radiation and hydrogen diffusion behavior, as well as its impact on the mechanical response of Zircaloy-2 cladding.

2. Theory

2.1 Hydrogen diffusion model

Generally, hydrogen diffuses into metals mainly through NILS diffusion, while dislocations act as trapping sites, along which diffusion can be neglected [32]. According to the work of Sofronis and McMeeking [10], the transported hydrogen resides at the NILS and dislocation is described as follows [10]:

$$\begin{cases} C_L = \theta_L \beta N_L, \\ C_T = \theta_T \alpha N_T, \end{cases} \tag{1}$$

where C_L represents the NILS hydrogen concentration; θ_L is the fraction of lattice sites occupied by hydrogen; β denotes the amount of interstitial sites per solvent atom (there exists one octahedral and two tetrahedral sites per atom in α-zirconium, such that $\beta = 3$); and $N_L = \rho_m N_A / M$ is solvent atomic density related to metal atom properties. In this study, $\rho_m = 6.49 \times 10^{-9}$ t/mm^3, is zirconium's density and M is zirconium's relative atomic mass, i.e., 9.1×10^{-5} t/mol [33]. C_T is the dislocation trapped hydrogen concentration; θ_T is the trapping sites occupancy ($0 \leqslant \theta_T \leqslant 1$); $\alpha = 1$, is the number of sites per trap; N_T denotes the number of sites per

trap. This value can be estimated by assuming that for every atomic plane intersected by a dislocation there is a trap, this value can be estimated [34]

$$N_T=\frac{\rho}{b}, \tag{2}$$

where b denotes the magnitude of the $a/3\ \langle 1120\rangle$ Burgers vector in HCP that equals the lattice constant a for zirconium; ρ is the dislocation density, and it depends on the accumulated plastic strain. In Refs. [10,13,35], fitting experimental data was a commonly used approach to establish the relationship between trap density and plastic strain. Similarly, through fitting the experimental data in Ref. [36], the dislocation density takes the form

$$\begin{cases} \rho = a\times(\varepsilon^P)^b, & \varepsilon^P < 0.5, \\ \rho = 2.894\times 10^8, \varepsilon^P \geqslant 0.5, \end{cases} \tag{3}$$

where $a = 4.7\times 10^8\ \mathrm{mm}^{-2}$; $b = 0.7$; and ε^P is the equivalent plastic. Substituting Eq. (3) into (2), the N_T-ε^P relation can be obtained.

Taking into account mass conservation, the rate of change of the total hydrogen concentration ($C = C_L + C_T$) in volume V equals the flux through its surface S. Therefore, the hydrogen diffusion equation is given by

$$\frac{\mathrm{d}}{\mathrm{d}t}\int_V C\mathrm{d}V+\int_S \mathbf{J}\cdot\mathbf{n}\mathrm{d}S = 0, \tag{4}$$

where $\mathbf{n}$ denotes the outer normal and $\mathbf{J}$ represents the hydrogen flux. The chemical potential gradient is considered as the driving force for the diffusion process. Additionally, for a system under external stress and at constant pressure and temperature, there is a functional relationship between chemical potential and hydrostatic stress, given by [10]

$$\mathbf{J} = -D_L\nabla C_L+\frac{D_L}{RT}C_L\overline{V}_H\nabla\sigma_H, \tag{5}$$

where R = 8.31 J/(mol·K), denotes the universal gas constant; T represents the temperature; $\overline{V}_H$ denotes the partial molar volume of hydrogen in metals; σ_H denotes the hydrostatic stress; and D_L represents the diffusion coefficient between NILS. Since the traps lack close proximity to one another and have binding energy restrictions, it is often believed that there is little hydrogen flux between them [5].

According to Oriani's theory [37], there exists a local equilibrium between hydrogen concentrations at NILS and traps ($\theta_L \ll 1$)

$$\begin{cases} \dfrac{\theta_T}{1-\theta_T} = K_T\theta_L, \\ K_T = \exp\left(-\dfrac{W_B}{RT}\right), \end{cases} \tag{6}$$

where W_B is the dislocation trap binding energy. According to the experiment conducted by Swan et al. [38], the binding energy between hydrogen atoms and dislocation was found to be 0.27 eV in Zircaloy. Based on Eqs. (1) and (6), C_T can be expressed as follows:

$$C_T = \frac{N_T K_T C_L}{K_T C_L + N_L}. \tag{7}$$

As shown in Eqs. (2) and (3), N_T is determined by the plastic strain. It is noted that the application of Oriani's theory reduces the number of unknown quantities, as C_T can be calculated once C_L is known. Taking into account the trap generation rate, the partial derivative of C_T is given by

$$\frac{\partial C_T}{\partial t} = \frac{\partial C_T}{\partial L}\frac{\partial C_L}{\partial t}+\theta_T\frac{\partial N_T}{\partial \varepsilon^P}\frac{\partial \varepsilon^P}{\partial t}. \tag{8}$$

Substituting Eqs. (5) and (8) into (4), one can obtain

$$\int_V\left[\frac{D_L}{D_{\mathrm{eff}}}\frac{\partial C_L}{\partial t}-\nabla\cdot\left(D_L\nabla C_L\right)+\nabla\cdot\left(\frac{D_L}{RT}C_L\overline{V}_H\nabla\sigma_H\right)\right.$$
$$\left.+\theta_T\frac{\partial N_T}{\partial\varepsilon^P}\frac{\partial\varepsilon^P}{\partial t}\right]\mathrm{d}V = 0, \tag{9}$$

where $D_{\mathrm{eff}} = D_L C_L\big/\left[C_L + C_T(1-\theta_T)\right]$ defines as the effective diffusion coefficient [39].

2.2 Constitutive law

Hydrogen diffusion equations include hydrostatic and equivalent plastic strain terms, so the influence of hydrogen on the material response should therefore be described by the constitutive equations. Tabata and Birnbaum [35] experimentally demonstrated that the local flow stress of the material decreases as the hydrogen pressure in the ambient cell increases. Besides, Birnbaum and Sofronis [40] stated that hydrogen-enhanced dislocation mobility leads to local softening. Therefore, the influence of the hydrogen softening effect on the yield stress σ_{ys} is described as [41]

$$\sigma_{\mathrm{ys}} = \Phi(C)\sigma_0\left(1+\frac{E}{\sigma_0}\varepsilon^p\right)^n, \tag{10}$$

where σ_0 denotes the initial yield stress; E is the modulus of elasticity; and n represents the hardening exponent that is assumed to be irrelevant to hydrogen. Equation (10) suggests that the hydrogen effect is achieved by the factor $\Phi(C)$

$$\Phi(C) = \xi C+1, \tag{11}$$

where ξ is the parameter of the coupled effect that determines the extent of hydrogen softening. It is worth to mention that an experimental fitting is still needed to afford the physical base of this parameter [42]. Hence, following Díaz et al. [42], it is assumed that at the maximum hydrogen concentration, ξ is chosen to achieve a 15% reduction in the initial yield stress.

Besides, the hydrogen atom induced lattice expansion is also considered, thus the total deformation rate tensor $\mathbf{D}_{ij}$ is

written as

$$\mathbf{D}_{ij} = \mathbf{D}_{ij}^{\mathrm{e}} + \mathbf{D}_{ij}^{\mathrm{p}} + \mathbf{D}_{ij}^{\mathrm{h}}, \tag{12}$$

where the components induced by hydrogen, plastic, and elastic are denoted by the superscripts h, p, and e, respectively. It is assumed that hydrogen causes pure dilatation, thus the corresponding term takes the form

$$\begin{cases} \mathbf{D}_{ij}^{\mathrm{h}} = \dfrac{\lambda}{3+\lambda(C-C_0)}\dfrac{\mathrm{d}c}{\mathrm{d}t}\delta_{ij}, \\ \lambda = \dfrac{\Delta v}{\Omega}, \end{cases} \tag{13}$$

where C_0 denotes the initial hydrogen concentration; parameter $\lambda = \Delta v/\Omega$, where Δv is the change in volume caused by each resided hydrogen atom, and Ω is the average volume of a zirconium atom.

2.3 The application of Direct FE^2 method in hydrogen diffusion analysis

Considering the coupled mechanical-diffusion system, a body with volume V bounded by a surface S, which consists of these parts: NILS concentration C_L on S_C and traction $\mathbf{t}$ on S_t, and the flux is $\mathbf{J}\cdot\mathbf{n} = \phi$ on S_ϕ ($\mathbf{n}$ is the normal to the outside). Since the concentration is known on S_C, the variation of C_L is $\delta C_L = 0$ on S_C. Therefore, the balance equations of the system in regard to the principle of virtual work is derived as (the body force is ignored)

$$\begin{aligned} &\int_V \left(\boldsymbol{\sigma} : \nabla\delta\mathbf{u} + \delta C_L D\dot{C}_L - \nabla\delta C_L\cdot\mathbf{J} + \delta C_L P\right)\mathrm{d}V \\ &= \int_{S_t} \mathbf{t}\cdot\delta\mathbf{u}\mathrm{d}S - \int_{S_\phi}\delta C_L\phi\mathrm{d}S, \end{aligned} \tag{14}$$

where $\boldsymbol{\sigma}$, $\mathbf{u}$, and $\mathbf{t}$ denote tensors of the stress, displacement, and tractions, respectively; $D = D_L/D_{\mathrm{eff}}$; and P can be expressed as [11]

$$P = \frac{\theta_T \mathrm{d}N_T \mathrm{d}\varepsilon^P}{\mathrm{d}\varepsilon^P \mathrm{d}t}. \tag{15}$$

In FE analysis, the left side of Eq. (14) can be rewritten in the form of numerical integration by Gaussian quadrature

$$\sum_e\sum_\alpha \omega_\alpha J_\alpha \left(\boldsymbol{\sigma} : \nabla\delta\mathbf{u} + \delta C_L D\dot{C}_L - \nabla\delta C_L\cdot\mathbf{J} + \delta C_L P\right)_\alpha, \tag{16}$$

where indices denote the integration point α in element e; ω_α and J_α are the weighting coefficient and the Jacobian, respectively, for the integration point. In Direct FE^2, an RVE is assigned to each integration point of the macroscale element, where Eq. (15) becomes

$$\sum_e\sum_\alpha \omega_\alpha J_\alpha \left\langle \tilde{\boldsymbol{\sigma}} : \tilde{\nabla}\delta\tilde{\mathbf{u}} + \delta\tilde{C}_L\tilde{D}\dot{\tilde{C}}_L - \tilde{\nabla}\delta\tilde{C}_L\cdot\tilde{\mathbf{J}} + \delta\tilde{C}_L\tilde{P}\right\rangle_\alpha, \tag{17}$$

where the superscript "~" and "⟨⟩" denote microscale quantities and volume average quantities over the RVE, respectively, which need to be transferred to the macroscale. To ensure energy consistency between the micro and macro scales, the information transformation must satisfy the Hill-Mandel homogenization condition. Regarding the issue of hydrogen diffusion, the extended form of the Hill-Mandel equation can be formulated as

$$\begin{aligned} &\sum_e\sum_\alpha \omega_\alpha J_\alpha \left\langle \tilde{\boldsymbol{\sigma}} : \tilde{\nabla}\delta\tilde{\mathbf{u}} + \delta\tilde{C}_L\tilde{D}\dot{\tilde{C}}_L - \tilde{\nabla}\delta\tilde{C}_L\cdot\tilde{\mathbf{J}} + \delta\tilde{C}_L\tilde{P}\right\rangle_\alpha \\ &= \sum_e\sum_\alpha \frac{\omega_\alpha J_\alpha}{|V_{\mathrm{RVE}}|}\int_{V_{\mathrm{RVE}}} \left(\tilde{\boldsymbol{\sigma}} : \tilde{\nabla}\delta\tilde{\mathbf{u}} + \delta\tilde{C}_L\tilde{D}\dot{\tilde{C}}_L - \tilde{\nabla}\delta\tilde{C}_L\cdot\tilde{\mathbf{J}} + \delta\tilde{C}_L\tilde{P}\right)\mathrm{d}V \\ &= \sum_e\sum_\alpha \omega_\alpha J_\alpha \left(\boldsymbol{\sigma} : \nabla\delta\mathbf{u} + \delta C_L D\dot{C}_L - \nabla\delta C_L\cdot\mathbf{J} + \delta C_L P\right)_\alpha, \end{aligned} \tag{18}$$

where the volume of the RVE is denoted by $|V_{\mathrm{RVE}}|$; the multiplication coefficient, $\dfrac{\omega_\alpha J_\alpha}{V_{\mathrm{RVE}}}$, is readily accommodated at the pre-processing stage by scaling the RVE's section thickness for 2D simulations, such that $V_{\mathrm{RVE}} = \omega_\alpha J_\alpha$.

Substituting Eq. (17) into (14), it yield

$$\begin{aligned} &\sum_e\sum_\alpha \frac{\omega_\alpha J_\alpha}{|V_{\mathrm{RVE}}|}\int_{V_\alpha} \left(\tilde{\boldsymbol{\sigma}} : \tilde{\nabla}\delta\tilde{\mathbf{u}} + \delta\tilde{C}_L\tilde{D}\dot{\tilde{C}}_L - \tilde{\nabla}\delta\tilde{C}_L\cdot\tilde{\mathbf{J}} + \delta\tilde{C}_L\tilde{P}\right) \\ &\mathrm{d}V = \int_{S_t} \mathbf{t}\cdot\delta\mathbf{u}\mathrm{d}S - \int_{S_\phi}\delta C_L\phi\mathrm{d}S. \end{aligned} \tag{19}$$

As can be seen in Eq. (19), the left side has been replaced by microscale quantities, while the right side maintains the macroscale description. Based on the built energetically consistent way, the macro and micro DOFs are linked to provide the macro–micro transition. Adopting PBCs, the nodal displacement filed $\mathbf{u}$ and the addition DOF of C_L take the form

$$\begin{cases} \left(\tilde{C}_L\right)_A - \left(\tilde{C}_L\right)_B = \nabla N_I(\mathbf{x}_0)\cdot(\mathbf{x}_A - \mathbf{x}_B)(C_L)_I, \\ \tilde{\mathbf{u}}_A - \tilde{\mathbf{u}}_B = \nabla N_I(\mathbf{x}_0)\cdot(\mathbf{x}_A - \mathbf{x}_B)\mathbf{u}_I, \end{cases} \tag{20}$$

where A and B indicate nodal pairs on opposite edges of the RVE; N_I represents the shape function at the macroscale; $\mathbf{x}_0$ locates the macroscopic element's integration point, coinciding with the center of the RVE; $\mathbf{x}_A$ and $\mathbf{x}_B$ are points within the macroscale element.

3. Implementation

Since the scarce versatility in Finite Element commercial codes, the coupled stress-diffusion analyses are usually solved by analogy with thermodynamic problems [5,42,43], and this methodology was adopted in this work. Actually, in Abaqus, the conduction-based heat transfer refers to the Fourier law, which fails to describe the hydrogen diffusion process shown in Eq. (5). Therefore, a user defined heat transfer model was implemented by the UMATHT sub-

routine, and the mechanical constitutive law is inserted by the UMAT subroutine. Additionally, according to the study of Díaz et al. [42], the analogy of the hydrogen-induced lattice expansion to the thermal dilatation expansion was implemented by the UEXPAN subroutine. Table 1 summarizes the definition of the variables used in heat transfer and hydrogen diffusion analysis (the initial hydrogen concentration, measured in hydrogen atoms per solvent atom, is represented by C and C_0. λ is the volumetric increase per induced hydrogen atom divided by the average atomic volume of the host metal atom.).

The implementation of Direct FE^2 method requires two steps and can be accomplished at the pre-processing stage. First, for a 2D simulation, the scaling is realized by changing the section thickness of the RVE without any side effects. Second, since drawing an analogy with the heat transfer problem, the DOF of the NILS concentration has been replaced by temperature. Therefore, the linking of the macroscale nodal temperature and displacement to the nodes at the boundaries of RVEs (Eq. (20)) is achieved by multi-point constraints in Abaqus. According to Eq. (19), the macroscale quantities are not evolved in the virtual work, thus the macro model is discretized into dummy elements with microscale RVEs superimposed on them. In addition, the RVE centroid is usually aligned with the integration point of the macroscopic element, although its location does not affect the calculation results.

Table 1 Analogies between heat transfer and hydrogen diffusion

Heat transfer	Hydrogen diffusion
Internal energy per unit mass $\widehat{U}$	Total concentration $C_L + C_T$
Temperature T	NILS concentration C_L
Hear flux $\mathbf{J}^{\phi}$	Hydrogen flux $\mathbf{J}$
Heat capacity c_{ϕ}	1
Density ρ	1
Thermal expansion coefficient α	$\alpha = \dfrac{\lambda}{3+\lambda(C-C_0)}$

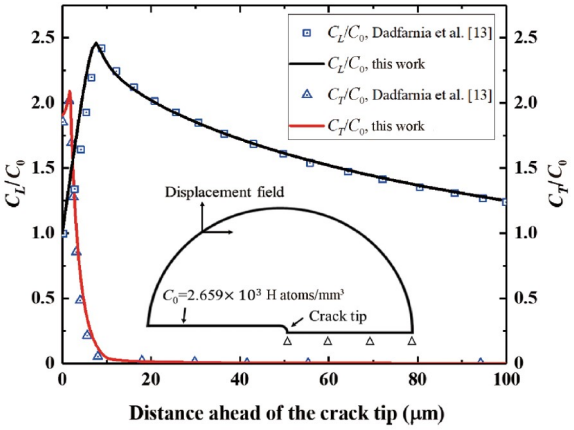

Figure 1 Hydrogen concentration at the lattice and trapping sites, compared with Ref. [13] (C_0 is the initial hydrogen concentration applied at the boundary).

4. Verification

The verification procedure includes two steps: validating the accuracy of the subroutine and the Direct FE^2 method to solve the hydrogen diffusion problem. Firstly, a simulation replicating the research of Dadfarnia et al. [13] was conducted using identical model and material parameters. As shown in Fig. 1, the concentration profiles are in good accordance with their results, verifying the correctness of the subroutine code. Secondly, the Direct FE^2 method undergoes performance evaluation by benchmarking it against direct numerical simulations (DNS). For an RVE, it is a square with a void located in the center and is discretized into 60 CPE4T coupled temperature-displacement elements. The Direct FE^2 model (Fig. 2(a)) consists of 2 macroscopic elements and 8 RVEs embedded at the integration points of the macroscopic elements, resulting in a total of 482 elements in the model. In comparison, the corresponding DNS model comprises 27000 elements with the same mesh size of the Direct FE^2 model. Both models utilize identical material parameters (listed in Table 2) and boundary conditions. Specifically, a hydrogen concentration boundary of $C_0 = 2.65 \times 10^{13}$ H·atoms/mm^3 is imposed on the left side of the model, while PBCs are implemented on the top and bottom surfaces to simulate uniaxial tensile testing. Coupled temperature-displacement (transient) analysis is utilized, with a displacement of 1 mm applied in the Y direction. After 10000 s, it can be seen in Fig. 2(b) and (c) that the Direct FE^2 method accurately captures both the hydrogen diffusion behavior and the elasto-plastic response of the model.

Moreover, the hybrid model was also built to further reduce the computational cost. This model includes one Direct FE^2 and two homogeneous macroscale elements, as shown in the inserts in Fig. 3. The effective Young's modulus and diffusion coefficient are calculated by a uniaxial tensile test on an RVE and assigned to the homogeneous macroscale elements, thus achieving equivalence to the Direct FE^2 element. The validation results are presented in Fig. 3(a) and (b). It is evident that the hybrid model accurately captures both the hydrogen diffusion behavior and the mechanical reaction. Besides, monitoring of computational efficiency showed that the Direct FE^2 simulation used 84.4 s of CPU time compared to 2673.2 s for the DNS.

5. Hydrogen diffusion in the Zircaloy-2 cladding tube

The inner and outer radii of the Zircaloy cladding tube served in Japanese pressurized water reactors are 4.18 mm

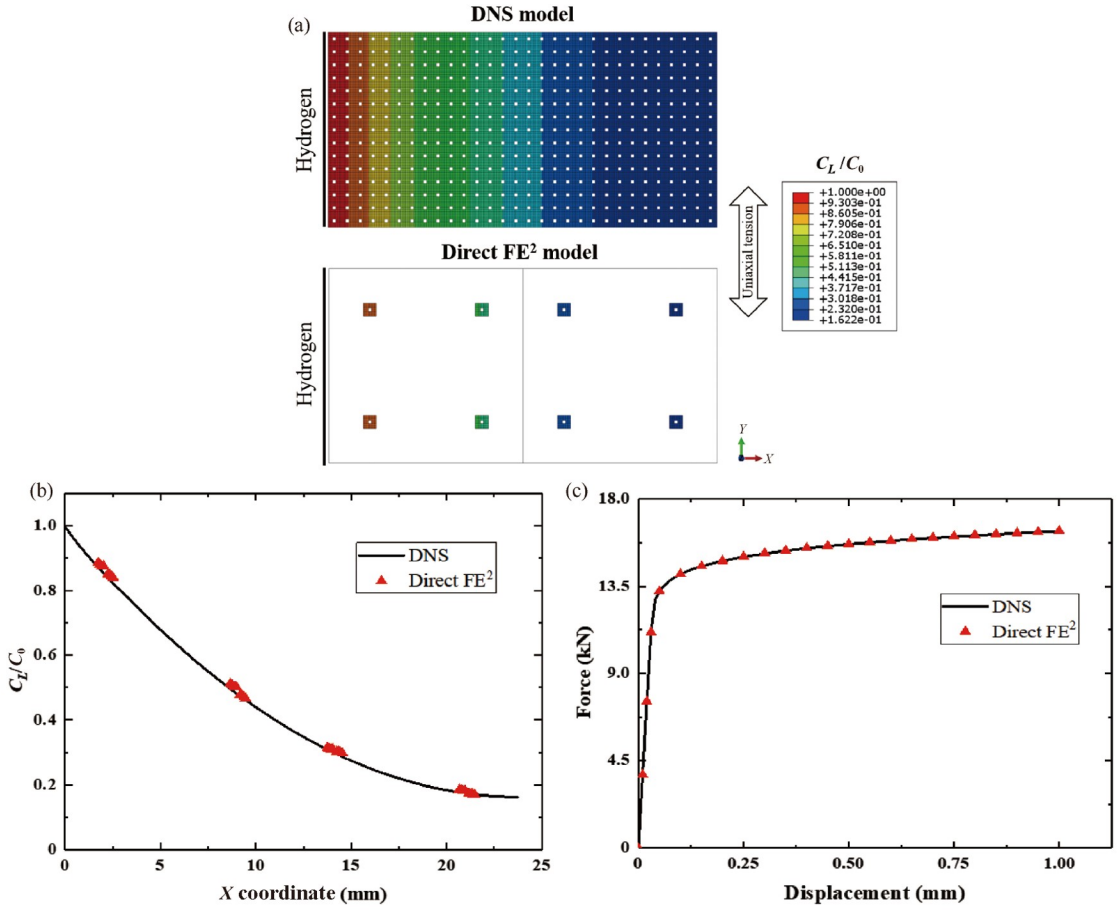

Figure 2 Validation of Direct FE^2 method.

Table 2 Material properties of Zircaloy-2

Parameter	Symbol	Value
Young's modulus (MPa)	E	99300
Poisson's ratio	μ	0.37
Initial yield stress (MPa)	σ_0	241
Work hardening exponent	n	0.2
Dislocation binding energy (mJ/mol)	W_B	2.61×10^7
Temperature (K)	T	293
Universal gas constant (mJ/(mol·K))	R	8314.5
Partial molar volume of H (mm^3/ mol)	$\overline{V}_H$	700
Diffusivity (mm^2/s)	D_L	1.74×10^{-7}

and 4.75 mm, respectively [44]. In this paper, the same dimensions are adopted to establish a 1/90 cross-sectional model. The hybrid Direct FE^2 modelling technique was utilized, and the side length of the square RVE was 0.002 mm with the element size of 0.00012 mm, compared to the size of 0.04 mm for the macroscale element. Although the released fission gas generates internal pressure inside the cladding tube, it is negligible in comparison to the primary circuit pressure acting on the external surface of the cladding [45]. Additionally, O-H bonds in the surface oxide layer can prevent hydrogen diffusion through it, and the path of movement for hydrogen is located at the micro-cracks formed by the dissolution of the oxide layer [46]. Therefore, in the model, the pressure is loaded on the external surface of the cladding, and a narrow crack was considered as the hydrogen surface, as illustrated in Fig. 4. To study the hydrogen diffusion rather than the precipitation behavior, the initial hydrogen concentration C_0 at the crack surface is given by 0.5 weight parts per million (2×10^{15} H·atoms/mm^3), which is lower than its solubility in Zircaloy (around 1 weight parts per million at room temperature [47]). In addition, in irradiation experiments, the observed dimension of the voids is up to several hundred nanometers [48]. Accordingly, without special instructions, the maximum dimension of the voids was set to below 200 nm in this work, and a model without any initial defectss was built as a benchmark for the Direct FE^2 model. The material properties of Zircaloy-2 are listed in Table 2 [38,49,50].

5.1 The influence of the voids on the hydrogen distribution

Initially, the domain is stress and hydrogen-free. Subsequently, both stress and hydrogen levels increase over 1 s

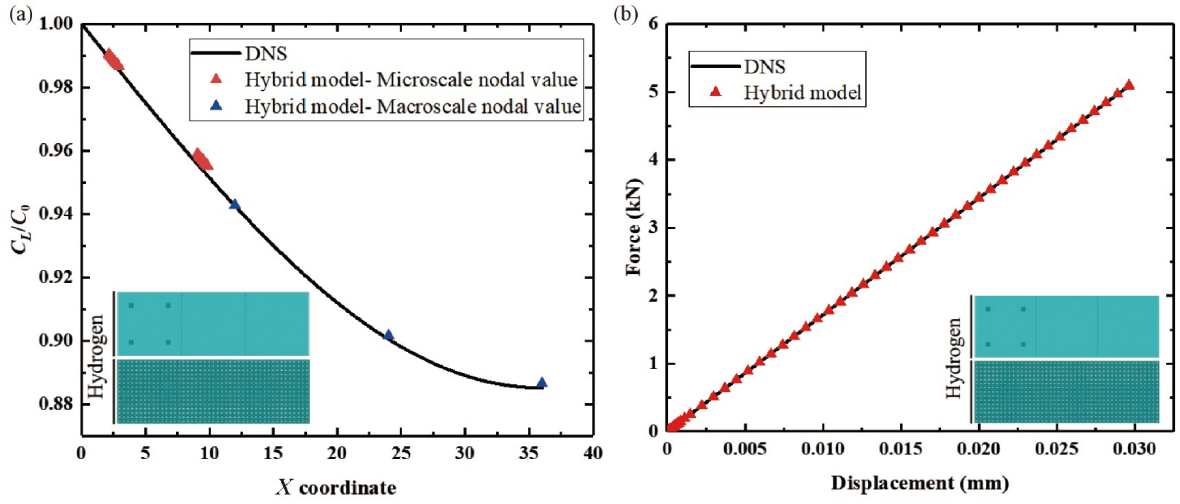

Figure 3 Validation of the hybrid Direct FE^2 method.

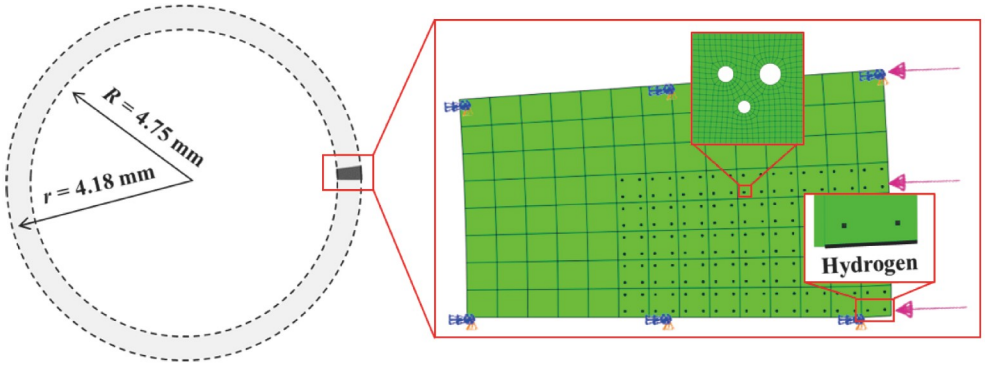

Figure 4 Direct FE^2 model of the Zircaloy cladding tube.

and remain constant thereafter. When a pressure of 30 MPa is applied to the external surface of the cladding, the NILS hydrogen concentration distribution near the crack tip is displayed in Fig. 5 for both the Direct FE^2 and reference models after 864000 s of diffusion. In the referential model, the NILS hydrogen concentration exhibits a concentric distribution centered on the crack surface, indicating uniform hydrogen diffusion from the crack surface into the cladding. Likewise, the NILS hydrogen concentration in the Direct FE^2 model shows a similar pattern, with hydrogen accumulating at the crack surface. The voids do not alter the overall path of hydrogen diffusion from the exterior surface towards the interior of the cladding.

According to Eq. (5), diffusion is propelled by gradients in concentration and hydrostatic stress. The hydrogen flux moves in a direction opposite to the concentration gradient but aligns with the hydrostatic stress gradient. As is known, hydrogen is generated by the zirconium-water corrosion reaction at the outer surface of the cladding; thus, the concentration gradient inside and outside the cladding inevitably leads to hydrogen invasion. To clarify the role of hydrostatic stress, its distribution in front of the crack tip is

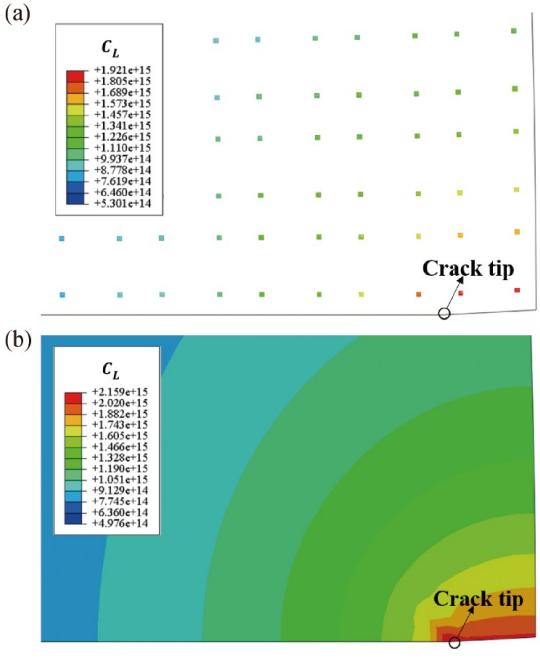

Figure 5 NILS hydrogen distribution in: (a) the Direct FE^2 model; (b) the referential intact model.

illustrated in Fig. 6. In the reference model, hydrostatic stresses are negative away from the crack surface, with the lowest (more negative) value occurring directly in front of the crack tip, as illustrated in the insert of Fig. 6. There is no doubt that the formed negative hydrostatic stress gradient prevents hydrogen from entering the cladding through the crack tip. Diffusion is driven entirely by the concentration gradient. Likewise, in the Direct FE^2 model, the mean hydrostatic stress in the RVEs ahead of the crack tip also exhibits a negative gradient, indicating the same driving force for picking up hydrogen. In Ref. [45], it was found that the maximum internal pressure caused by the released fission gas in the cladding was 0.59 MPa. Additionally, numerical cases were supplemented to account for the additional internal pressure induced by the irradiation swelling of the pellets, with internal pressures of 5 MPa. As shown in Fig. 6, under all loading conditions, a negative hydrostatic stress gradient was produced around the crack. Therefore, a competitive relationship exists between the concentration gradient and hydrostatic stress gradient in influencing the hydrogen diffusion process. All observed hydrogen diffusion in Zircaloy cladding can be attributed to the overwhelming effect of the concentration gradient.

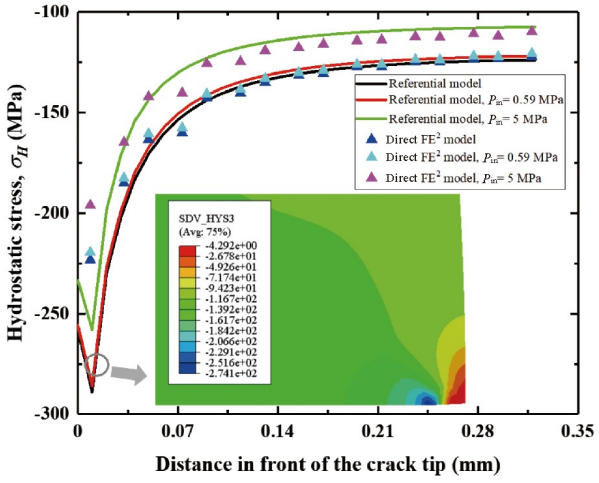

Figure 6 Hydrostatic stress distribution in front of the crack tip.

Although the same mechanism leads to similar hydrogen diffusion processes in both models, the microscale diffusion behavior in RVEs still exhibits traits dependent on microdefects. In Fig. 7, the contour lines of the NILS concentration delineate the diffusion direction from the bottom right corner to the top left corner. However, it is evident that in areas A, B, and C, the contour lines bend significantly toward the void. These areas have a common feature, that is, the hydrostatic stress changes most dramatically, which means that there is the highest hydrostatic stress gradient here. Comparison with the uniform diffusion in the referential model (Fig. 5(b)) suggests that the high hydrostatic stress gradient region around the micro-voids leads to nonuniform microscopic diffusion properties.

The distribution of the trapped hydrogen concentration is shown in Fig. 8. It is evident that C_T increases with diffusion time and achieves its maximum value near the crack tip in both models. However, the value of C_T is always higher in the Direct FE^2 model. Besides, at the area far from the crack tip, C_T is directly zeroed in the referential model, while it gradually decreases as the distance from the crack tip increases in the other model. This can be explained by the fact that, in the referential model, only a small scale yielding zone occurs around the crack tip. In contrast, the presence of micro-voids results in a larger yielding area in the Direct FE^2 model. Plastic deformation causes dislocation proliferation, leading to an increase in dislocation traps. As hydrogen atoms are continuously transported from the crack tip, traps will gradually fill up over time, leading to a higher value of C_T. During straining, in the Direct FE^2 model, plastic strain bands as well as high-density dislocation traps appear at the inter-void ligament, where eventually becomes the region of localized hydrogen accumulation, as shown in Fig. 9. In this plot, the similar distribution profiles of C_T and ε^P originate

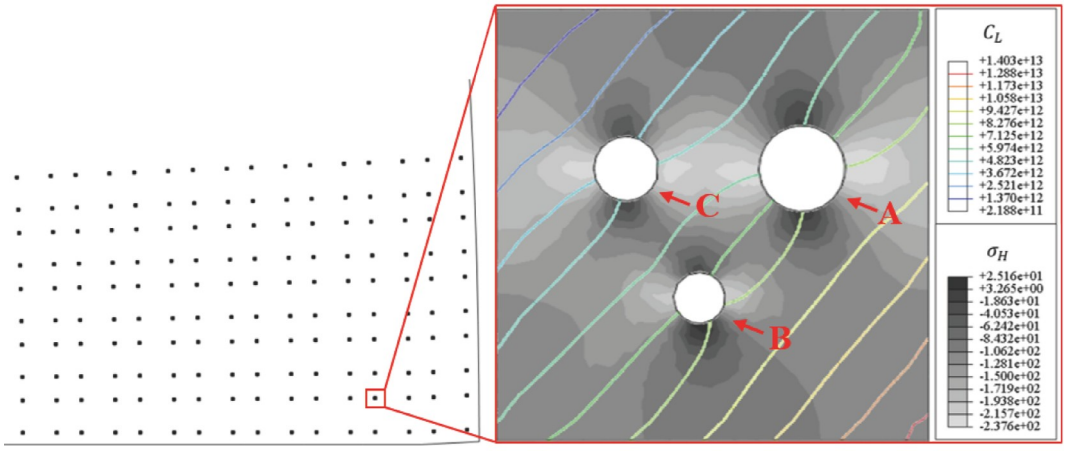

Figure 7 NILS hydrogen and hydrostatic stress distributions in the RVE.

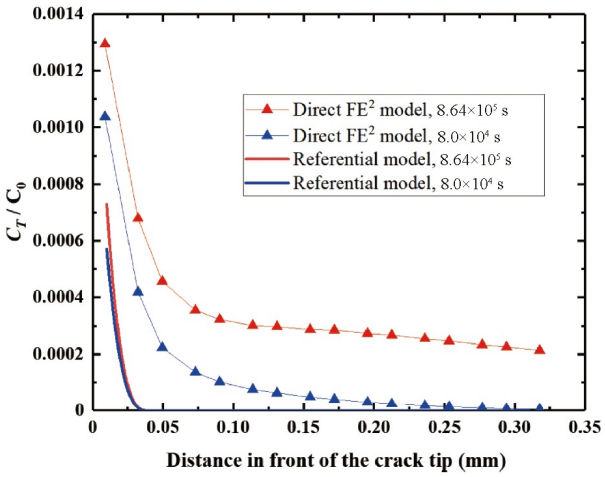

Figure 8 Tapped hydrogen concentration in front of the crack tip.

from their proportional relationship directed by Eq. (8). Taking into account the hydrogen-induced softening, the locally accumulated hydrogen will benefit the shear localization at the inter-void ligament, thereby promoting void coalescence. Moreover, it is believed that dislocations can act as conduits for hydrogen transport, facilitating its migration to the interior of the cladding at a much faster rate than lattice diffusion [51,52]. Furthermore, in Zircaloy, the dislocation traps are reversible due to the binding energy of the dislocation trap being 0.27 eV [44], indicating that the hydrogen atom can escape from the trap. This provides another efficient pathway for hydrogen to penetrate the depths of the cladding wall. As a result, the possibility of hydrogen-induced cladding damage is increased when trapped hydrogen is present.

In Fig. 10, both models show that the NILS hydrogen concentration in front of the crack tip gradually drops with distance, which is consistent with the distribution characteristics driven by concentration gradients. Moreover, the Direct FE^2 model exhibits a relatively higher NILS concentration after 80000 s of diffusion. However, when the diffusion proceeds to 864000 s, it becomes clear that, except for the region near the crack tip, the value of C_L is lower than that in the referential model. This phenomenon can be attributed to the existence of trapping sites, which to some extent reduce hydrogen diffusivity. Specifically, the ratio of effective diffusivity to lattice diffusivity is plotted in Fig. 11, revealing a reverse correlation between dislocation density and effective diffusivity. According to the definition of D_{eff} in Eq. (9), when hydrogen atoms, which should participate in lattice diffusion, are captured by high-density inter-void dislocation traps, effective diffusivity inevitably decreases in the Direct FE^2 model. Therefore, near the crack tip, due to the low effective diffusivity, hydrogen atoms entering the model accumulate near the crack tip and are difficult to transport to the depth of the cladding wall, resulting in a locally higher C_L value. Nevertheless, the lower C_L in Direct FE^2 model, at the area far from the crack tip, in addition to the lower effective diffusivity, can also be attributed to the competition between the trapping effect and the NILS diffusion. The mean NILS occupation in the RVE furthest from the crack is calculated to be $\theta_L = 1.39 \times 10^{-6}$, while the trap occupation is $\theta_T = 5.92 \times 10^{-2}$, which is larger by a factor of around forty thousand compared to θ_L. This implies that once the hydrogen atoms arrive, the dislocation trap will be preferentially filled. Hence, the overwhelming trapping effect is also responsible for the higher C_T in Fig. 8 and the lower C_L in Fig. 10.

5.2 Hydrogen influence on void evolution

In the irradiation conditions, a large number of movable vacancies aggregate into clusters, which provides a nucleation site for voids. Subsequently, dispersed small voids undergo a process of growing and coalescing to form larger voids [53]. These represent two critical stages in the void evolution process. To investigate the influence of hydrogen on this process, two RVEs were established to characterize the distribution characteristics of voids at two typical stages

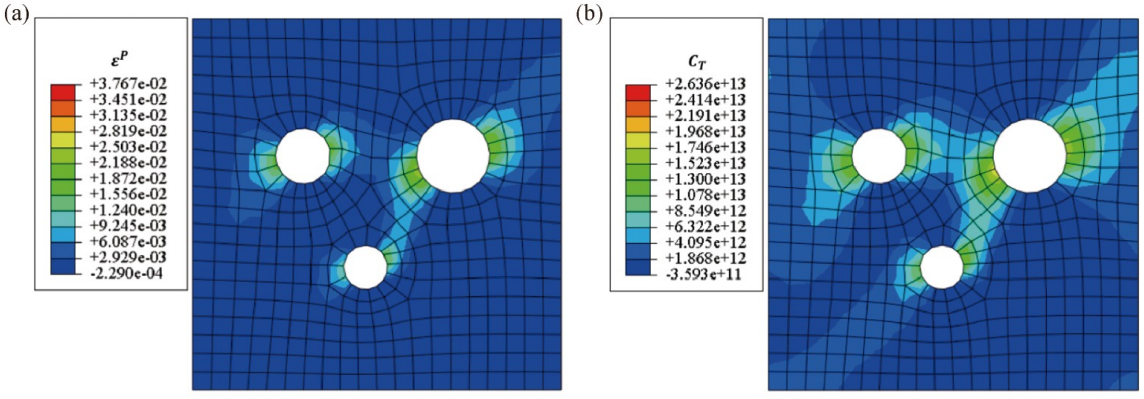

Figure 9 Contours of (a) equivalent plastic strain and (b) the trapped hydrogen concentration.

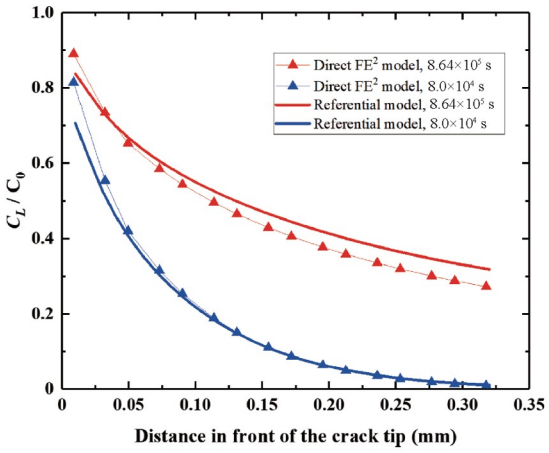

Figure 10 NILS concentration hydrogen concentration in front of the crack tip.

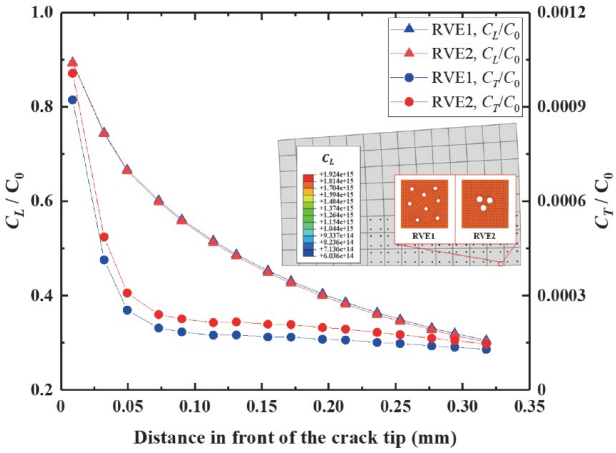

Figure 12 NILS and trapped concentration in front of the crack tip.

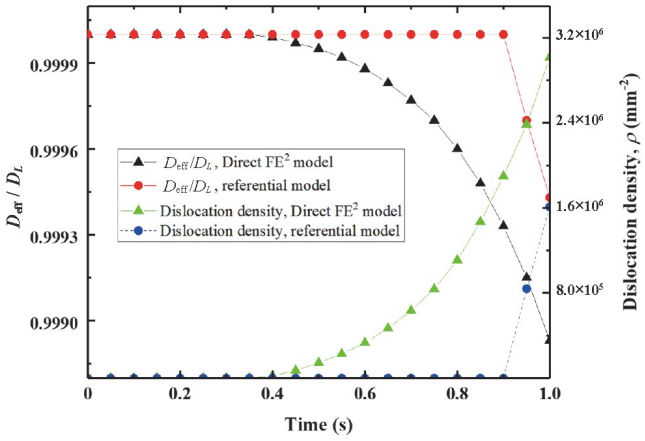

Figure 11 Evolution of the effective diffusivity and the dislocation density.

of void evolution: RVE1 has a large number of scattered small voids, and RVE2 is characterized by tightly distributed larger size voids. The void volume fraction in both RVEs is 4%. The variables related to the two RVEs are denoted by the subscripts ()1 and ()2, respectively.

Although the localized hydrostatic stress gradient causes non-uniform diffusion in RVEs, the diffusion driven by predominant concentration gradients eventually results in a uniform NILS hydrogen concentration distribution in both models after a sufficiently long period of diffusion, as illustrated in Fig. 12. However, it is notable that C_T is always higher in RVE2 along the crack tip. Essentially, diffusion propelled by the concentration gradient renders the NILS concentration distribution unaffected by the microstructure, whereas the microstructure solely influences the trapped concentration. Focusing on the RVE closest to the crack tip, as illustrated in Fig. 13, in RVE2, a significant accumulation of trapped hydrogen atoms occurs between the voids, resulting in a heightened local concentration. By contrast, in RVE1, fewer trapped hydrogen atoms are comparatively dispersed around the voids, while a trapped hydrogen concentration band interlinks the voids to form a network. Since the position of the trapped hydrogen coincides with the position of the dislocation accumulation, the observed disparity in C_T distribution between RVE1 and RVE2 reflects discrepancies in the distribution of the dislocation accumulation. Specifically, in comparison to RVE1, the voids in RVE2 are larger with closer spacing, resulting in heightened stress concentration between them, thereby promoting dislocation nucleation. Moreover, the confined area enclosed by the void surface impedes dislocation movement, leading

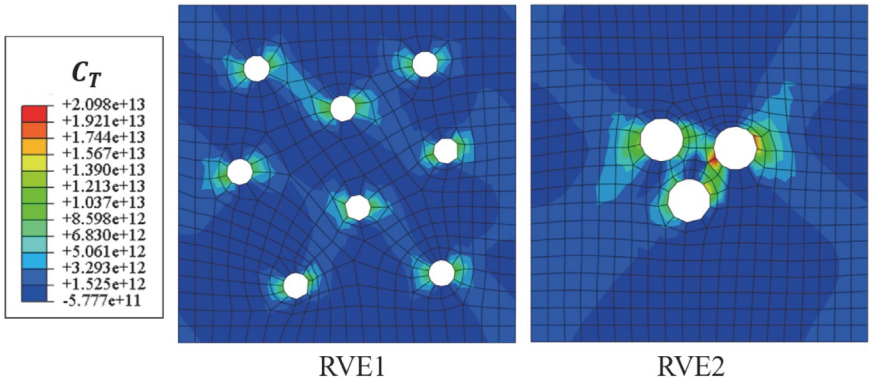

Figure 13 Distribution of trapped hydrogen concentration in RVEs.

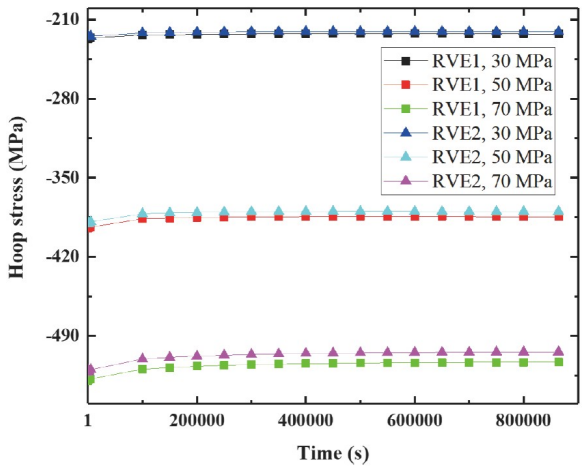

Figure 14 Hoop stress with different pressures applied on the cladding.

to a significant accumulation of dislocations and consequently trapping more hydrogen atoms. The differing trapped concentrations in RVE1 and RVE2 inevitably result in distinct mechanical responses of the macrostructure. The gradual decrease in hoop stress in the cladding observed in Fig. 14, despite constant hydrogen concentration and pressure at the boundary after being loaded for 1 s, is attributed to the hydrogen-induced softening effect. Notably, the Direct FE^2 model with RVE2 exhibits a more pronounced softening effect than the Direct FE^2 model with RVE1, with the gap between the two further widening as pressure gradually increases. This indicates that when void evolution in Zircaloy cladding enters the second stage, the heightened trapping of hydrogen atoms renders the cladding more sensitive to pressure changes. Consequently, the microstructure is more prone to reaching critical plastic deformation, leading to micro-crack initiation.

While extensive research has primarily focused on the hydrogen embrittlement phenomenon caused by hydrides in Zircaloy, experimental validation has confirmed the occurrence of hydrogen-induced softening in these alloys [54]. To investigate the influence of hydrogen-induced softening effect on void evolution, three different initial hydrogen concentrations were set. As illustrated in Fig. 15(a), it is evident that when the parameter C_0 is zero, plastic deformation occurs on both flanks of every void within RVE1, showcasing only one shear band interlinking the two voids positioned at the upper left corner. As C_0 increases to 1×10^{15} H atoms/mm^3, the dispersed voids become connected by a network of mild shear bands. Subsequently, when C_0 increases to 2×10^{15} H atoms/mm^3, the position of the shear band does not change, but it becomes more intense. In comparison, in Fig. 15(b), as C_0 increases from 0 to 2×10^{15} H atoms/mm^3, the plastic strain always concentrates at the inter-void ligament, with only a limited degree of range expansion. It is worth noting that all boundaries of the RVE are assigned PBCs, therefore the depicted distribution of plastic strain in the figure indicates little interaction between adjacent void clusters, which is a manifestation of significant plastic deformation localization. The hydrogen-induced softening effect observed in Fig. 15 can be attributed to the fact that plastic deformation primarily occurs through slip along slip lines and shear bands. Consequently, as slip begins, the hydrogen concentration at these slip lines

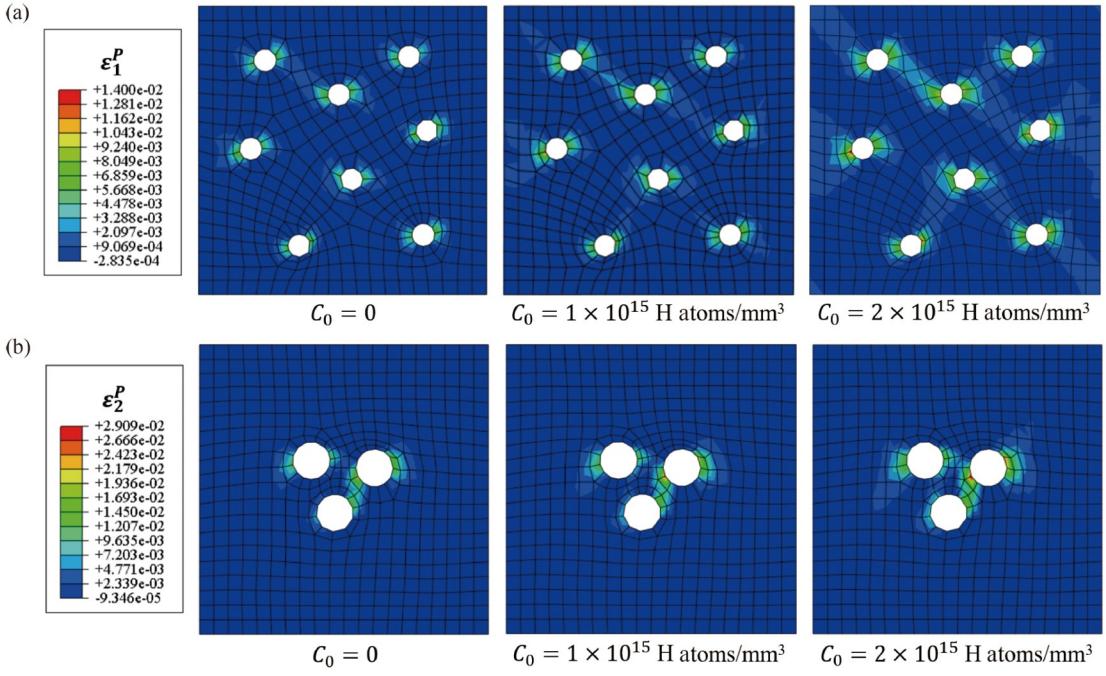

Figure 15 Distribution of plastic strain in (a) RVE1 and (b) RVE2 with different hydrogen boundary conditions.

or bands grows because hydrogen gets trapped at the dislocations. As the local hydrogen concentration rises, the material experiences localized softening, thereby enhancing shear localization [55]. The distinctive distribution of plastic strain depicted in Fig. 15(a) and (b) suggests that the hydrogen-induced softening effect has varying impacts on void evolution at different stages. In specific, the shear bands linking dispersed voids can cause distant voids to coalesce, a phenomenon known as the internal shearing void coalescence mode [56]. On the other hand, the highly localized plastic strain occurring between closely spaced large voids promotes the contraction of the inter-void ligament, leading to the so-called internal necking void coalescence mode [57]. The failure caused by these two types of void coalescence modes is known as internal shearing failure and internal necking failure, respectively [23]. Therefore, at the early phase of void evolution, the micro voids array exists in the matrix, and the shear bands linking void wide apart provide potential crack paths. Once cracking initiates, internal shearing is likely to induce cracks to propagate deep into the wall of the Zircaloy cladding. However, due to limited interaction with adjacent void clusters, internal necking is more prone to causing localized damage, potentially becoming the site of void nucleation.

6. Conclusions

This paper employs the Direct FE^2 method to address the multiscale hydrogen diffusion problem. The influence of micro-voids on hydrogen diffusion behavior and the effects of hydrogen on void evolution was investigated. The principal conclusions derived from the research findings are presented below:

(1) While the local hydrostatic pressure gradient induced by micro-voids causes microscopic non-uniform diffusion of hydrogen, the presence of micro-voids within the Zircaloy cladding has no influence on the NILS hydrogen distribution under the diffusion driven by predominant concentration gradients. However, there is a strong correlation between the trapped concentration and the microstructure.

(2) The accumulation of dislocations at the inter-void ligaments leads to the accumulation of trapped hydrogen, inducing localized plastic deformation, while also diminishing the effective diffusivity of hydrogen in the matrix.

(3) As the hydrogen concentration increases, at the early stages of void evolution, the hydrogen-induced softening effect initiates the formation of shear bands connecting widely spaced voids, thus facilitating the propagation of cracks deep into the wall of the Zircaloy cladding. As void evolution progresses into the second stage, characterized by the presence of large and closely spaced voids in the matrix, the hydrogen-induced softening effect enhances the occurrence of localized damage at the narrow inter-void ligaments.

Conflict of interest *On behalf of all authors, the corresponding author states that there is no conflict of interest.*

Author contributions ***Han Zhao:*** *Investigation, Methodology, Visualization, Funding acquisition, Writing – original draft.* ***Xianghua Zheng:*** *Methodology, Validation, Writing – review & editing.* ***Shiting Yang:*** *Methodology, Validation, Writing – review & editing.* ***Xin Yang:*** *Conceptualization, Methodology, Writing – review & editing.* ***Wei Li:*** *Project administration, Methodology, Writing – review & editing.*

Acknowledgements *This work was supported by the National Natural Science Foundation of China (Grant No. 52301131), Natural Science Foundation of Sichuan, China (Grant No. 2023NSFSC0908), and Research Foundation for Talents of Chengdu Technological University (Grant No. 2023RC017).*

1 Y. Deng, H. Liao, Y. He, Y. Yin, M. Pellegrini, G. Su, K. Okamoto, and Y. Wu, Investigation on hydrogen embrittlement and failure characteristics of Zr-4 cladding based on the GTN method, Nucl. Mater. Energy **36**, 101463 (2023).
2 A. Jha, N. Duhan, I. V. Singh, B. K. Mishra, R. Singh, and R. N. Singh, Numerical study of the hydride embrittlement in zirconium alloy using XFEM, Int. J. Str. Stab. Dyn. 2440002 (2023). doi: 10.1142/S0219455424400029.
3 X. H. Lin, I. J. Beyerlein, and W. Z. Han, Annealing cracking in Zr and a Zr-alloy with low hydrogen concentration, J. Mater. Sci. Tech. **182**, 165 (2024).
4 R. Ma, C. Liu, and X. Zhang, Repair of embrittlement induced by different hydride configurations by dissolving partial hydrides using pulsed electric current, Int. J. Hydrogen Energy **50**, 66 (2024).
5 O. Barrera, E. Tarleton, H. W. Tang, and A. C. F. Cocks, Modelling the coupling between hydrogen diffusion and the mechanical behaviour of metals, Comput. Mater. Sci. **122**, 219 (2016).
6 L. F. Wang, X. Shu, D. Y. Lin, G. H. Lu, and H. F. Song, Molecular dynamics studies of hydrogen diffusion in tungsten at elevated temperature: Concentration dependence and defect effects, Int. J. Hydrogen Energy **45**, 822 (2020).
7 R. Skelton, X. W. Zhou, and R. A. Karnesky, Molecular dynamics studies of lattice defect effects on tritium diffusion in zirconium, J. Nucl. Mater. **555**, 153099 (2021).
8 X. Wang, C. Xu, S. Hu, H. Xiao, X. Zhou, and S. Peng, First-principles calculation on the structure stability, hydrogen trapping behaviour, and adhesion properties of the Zr(0001) ZrC(100) interface, Appl. Surf. Sci. **508**, 144825 (2020).
9 B. Xing, R. Gao, M. Wu, H. Wei, S. Chi, and Z. Hua, Differentiation on crystallographic orientation dependence of hydrogen diffusion in α-Fe and γ-Fe: DFT calculation combined with SKPFM analysis, Appl. Surf. Sci. **615**, 156395 (2023).
10 P. Sofronis, and R. M. McMeeking, Numerical analysis of hydrogen transport near a blunting crack tip, J. Mech. Phys. Solids **37**, 317 (1989).
11 A. H. M. Krom, R. W. J. Koers, and A. Bakker, Hydrogen transport near a blunting crack tip, J. Mech. Phys. Solids **47**, 971 (1999).
12 A. H. M. Krom, and A. Bakker, Hydrogen trapping models in steel, Metall. Mater. Trans. B **31**, 1475 (2000).
13 M. Dadfarnia, P. Sofronis, and T. Neeraj, Hydrogen interaction with multiple traps: Can it be used to mitigate embrittlement? Int. J. Hydrogen Energy **36**, 10141 (2011).
14 E. Martínez-Pañeda, A. Golahmar, and C. F. Niordson, A phase field

formulation for hydrogen assisted cracking, Comput. Methods Appl. Mech. Eng. **342**, 742 (2018).
15 J. Y. Wu, T. K. Mandal, and V. P. Nguyen, A phase-field regularized cohesive zone model for hydrogen assisted cracking, Comput. Methods Appl. Mech. Eng. **358**, 112614 (2020).
16 H. Zhao, X. Zeng, X. Yang, W. Chen, and J. Wu, Investigation of the temperature effect on the primary radiation damage near the grain boundary in tungsten using Molecular dynamics simulations, Nucl. Instrum. Meth. B **476**, 32 (2020).
17 M. Nagumo, Hydrogen related failure of steels—A new aspect, Mater. Sci. Tech. **20**, 940 (2004).
18 X. C. Ren, Q. J. Zhou, W. Y. Chu, J. X. Li, Y. J. Su, and L. J. Qiao, The mechanism of nucleation of hydrogen blister in metals, Chin. Sci. Bull. **52**, 2000 (2007).
19 E. Maire, S. Grabon, J. Adrien, P. Lorenzino, Y. Asanuma, O. Takakuwa, and H. Matsunaga, Role of hydrogen-charging on nucleation and growth of ductile damage in austenitic stainless steels, Materials **12**, 1426 (2019).
20 J. Koplik, and A. Needleman, Void growth and coalescence in porous plastic solids, Int. J. Solids Struct. **24**, 835 (1988).
21 D. C. Ahn, P. Sofronis, and R. H. Dodds, On hydrogen-induced plastic flow localization during void growth and coalescence, Int. J. Hydrogen Energy **32**, 3734 (2007).
22 Y. Liang, D. C. Ahn, P. Sofronis, R. H. Dodds Jr., and D. Bammann, Effect of hydrogen trapping on void growth and coalescence in metals and alloys, Mech. Mater. **40**, 115 (2008).
23 H. Yu, J. S. Olsen, J. He, and Z. Zhang, Hydrogen-microvoid interactions at continuum scale, Int. J. Hydrogen Energy **43**, 10104 (2018).
24 J. P. Bandstra, and D. A. Koss, Modeling the ductile fracture process of void coalescence by void-sheet formation, Mater. Sci. Eng.-A **319-321**, 490 (2001).
25 R. J. M. Smit, W. A. M. Brekelmans, and H. E. H. Meijer, Prediction of the mechanical behavior of nonlinear heterogeneous systems by multi-level finite element modeling, Comput. Methods Appl. Mech. Eng. **155**, 181 (1998).
26 F. Feyel, and J. L. Chaboche, FE^2 multiscale approach for modelling the elastoviscoplastic behaviour of long fibre SiC/Ti composite materials, Comput. Methods Appl. Mech. Eng. **183**, 309 (2000).
27 H. Dang, P. Liu, Y. Zhang, Z. Zhao, L. Tong, C. Zhang, and Y. Li, Theoretical prediction for effective properties and progressive failure of textile composites: A generalized multi-scale approach, Acta Mech. Sin. **37**, 1222 (2021).
28 S. Zhao, J. Zhao, and Y. Lai, Multiscale modeling of thermo-mechanical responses of granular materials: A hierarchical continuum-discrete coupling approach, Comput. Methods Appl. Mech. Eng. **367**, 113100 (2020).
29 S. Zhao, H. Chen, and J. Zhao, Multiscale modeling of freeze-thaw behavior in granular media, Acta Mech. Sin. **39**, 722195 (2023).
30 K. Raju, T. E. Tay, and V. B. C. Tan, A review of the FE^2 method for composites, Multiscale Multi. Mod. **4**, 1 (2021).
31 J. Xu, P. Li, L. H. Poh, Y. Zhang, and V. B. C. Tan, Direct FE^2 for concurrent multilevel modeling of heterogeneous thin plate structures, Comput. Methods Appl. Mech. Eng. **392**, 114658 (2022).
32 E. Elmukashfi, E. Tarleton, and A. C. F. Cocks, A modelling framework for coupled hydrogen diffusion and mechanical behaviour of engineering components, Comput. Mech. **66**, 189 (2020).
33 A. Tondro, M. Taherijam, and H. Abdolvand, Diffusion and redistribution of hydrogen atoms in the vicinity of localized deformation zones, Mech. Mater. **177**, 104544 (2023).
34 F. Yang, W. Zhan, T. Yan, H. Zhang, and X. Fang, Numerical analysis of the coupling between hydrogen diffusion and mechanical behavior near the crack tip of titanium, Math. Problems Eng. **2020**, 1 (2020).
35 T. Tabata, and H. K. Birnbaum, Direct observations of the effect of hydrogen on the behavior of dislocations in iron, Scripta Metall. **17**, 947 (1983).
36 X. C. Song, W. Li, and L. Walters, The effect of cold work on irradiation creep of Zircaloy-2 alloys at low temperature, J. Nucl. Mater. **572**, 154086 (2022).
37 R. A. Oriani, The diffusion and trapping of hydrogen in steel, Acta Metall. **18**, 147 (1970).
38 H. Swan, P. Styman, H. Wilcox, N. Bowden, T. Ungar, L. Connor, A. Garner, A. Cole-Baker, P. Binks, C. Smith, S. Sikotra, J. Hawes, and S. Ortner, Measurement of hydrogen trapping in cold-work dislocations using synchrotron X-ray diffraction, J. Nucl. Mater. **571**, 154012 (2022).
39 R. Fernández-Sousa, C. Betegón, and E. Martínez-Pañeda, Analysis of the influence of microstructural traps on hydrogen assisted fatigue, Acta Mater. **199**, 253 (2020).
40 H. K. Birnbaum, and P. Sofronis, Hydrogen-enhanced localized plasticity—A mechanism for hydrogen-related fracture, Mater. Sci. Eng.-A **176**, 191 (1994).
41 H. Kotake, R. Matsumoto, S. Taketomi, and N. Miyazaki, Transient hydrogen diffusion analyses coupled with crack-tip plasticity under cyclic loading, Int. J. Pres. Ves. Pip. **85**, 540 (2008).
42 A. Díaz, J. M. Alegre, and I. I. Cuesta, Coupled hydrogen diffusion simulation using a heat transfer analogy, Int. J. Mech. Sci. **115-116**, 360 (2016).
43 F. Farukh, L. G. Zhao, N. C. Barnard, M. T. Whittaker, and G. McColvin, Computational modelling of full interaction between crystal plasticity and oxygen diffusion at a crack tip, Theor. Appl. Fract. Mech. **96**, 707 (2018).
44 F. Nagase, and T. Fuketa, Investigation of hydride rim effect on failure of Zircaloy-4 cladding with tube burst test, J. Nucl. Sci. Tech. **42**, 58 (2005).
45 U. K. Viswanathan, D. N. Sah, B. N. Rath, and S. Anantharaman, Measurement of fission gas release, internal pressure and cladding creep rate in the fuel pins of PHWR bundle of normal discharge burnup, J. Nucl. Mater. **392**, 545 (2009).
46 S. Suman, M. K. Khan, M. Pathak, R. N. Singh, and J. K. Chakravartty, Hydrogen in Zircaloy: Mechanism and its impacts, Int. J. Hydrogen Energy **40**, 5976 (2015).
47 C. M. Silva, F. Ibrahim, E. G. Lindquist, J. W. McMurray, and C. D. Bryan, Brittle nature and the related effects of zirconium hydrides in Zircaloy-4, Mater. Sci. Eng.-A **767**, 138396 (2019).
48 V. I. Pastukhov, I. A. Portnykh, and M. L. Lobanov, Effect of Mesostructural Elements on Radiation-Induced Porosity in 16Cr-19Ni-2Mo-2Mn-Nb-Ti-V-P-B Austenitic Steel, MSF **946**, 357 (2019).
49 C. L. Whitmarsh, Review of Zircaloy-2 and Zircaloy-4 properties relevant to NS Savannah reactor design, Technical Report (Oak Ridge National Laboratory for the US Atomic Energy Commission, 1962).
50 Z. Xia, B. Wang, J. Zhang, S. Ding, L. Chen, H. Pang, and X. Song, Three-dimensional numerical simulation of hydrogen-induced multi-field coupling behavior in cracked Zircaloy cladding tubes, Nucl. Eng. Tech. **51**, 238 (2019).
51 I. M. Robertson, H. K. Birnbaum, and P. Sofronis, Chapter 91 hydrogen effects on plasticity, Dislocations in Solids **15**, 249 (2009).
52 J. Tien, A. W. Thompson, I. M. Bernstein, and R. J. Richards, Hydrogen transport by dislocations, Metall. Trans. A **7**, 821 (1976).
53 Z. Sun, T. Guo, K. I. Elkhodary, H. Yang, N. Zhou, and S. Tang, Localization and macroscopic instability in nanoporous metals, Acta Mech. Sin. **38**, 121538 (2022).
54 S. Yamanaka, D. Setoyama, H. Muta, M. Uno, M. Kuroda, K. Takeda, and T. Matsuda, Characteristics of zirconium hydrogen solid solution, J. Alloys Compd. **372**, 129 (2004).
55 Y. Liang, P. Sofronis, and N. Aravas, On the effect of hydrogen on

plastic instabilities in metals, Acta Mater. **51**, 2717 (2003).
56 A. Pineau, A. A. Benzerga, and T. Pardoen, Failure of metals I: Brittle and ductile fracture, Acta Mater. **107**, 424 (2016).
57 A. Premono, and H. Kanayama, Characterization of void coalescence in alpha-iron in the presence of hydrogen, J. Comput. Sci. Tech. **7**, 395 (2013).

锆合金包壳中氢扩散的直接FE^{2}方法多尺度模拟

赵晗, 郑向华, 杨诗婷, 杨鑫, 李伟

摘要 本文基于直接FE^{2}方法, 提出多尺度模拟算法对锆合金包壳中的氢扩散行为进行了研究. 该算法利用降尺度规则和缩放因子将两个尺度的有限元计算纳入单一计算框架. 研究结果表明, 微孔洞会引起氢沿晶格的非均匀扩散, 而微孔洞分布将影响位错陷阱中的氢浓度. 随着位错中氢浓度增加, 局部塑性变形增加, 氢在锆合金中的有效扩散率降低. 此外, 建立了两种代表性体积单元, 分别体现孔洞演化过程不同阶段的分布特征. 计算结果表明, 在孔洞演化初期, 氢致软化效应促进裂纹往锆合金包壳内部扩展. 而在孔洞演化的第二阶段, 氢致软化效应则会诱导产生孔洞间隙局部损伤.